A Novel Fully Electronic Active Real-Time Imager Based on a Planar Multistatic Sparse Array

Sherif Sayed Ahmed, *Member, IEEE,* Andreas Schiessl, and Lorenz-Peter Schmidt, *Senior Member, IEEE*

Abstract—The interest in active millimeter-wave and microwave imaging systems is increasing due to their utilization in security, medical, and industrial applications. Imaging systems using monostatic arrays suffer from the high number of antenna positions, making a fully electronic solution very costly and impractical. Multistatic arrays, however, offer the chance for high reduction factors in the number of antennas, and then allow for fully electronic solutions. Here, a new array architecture is presented, which is suitable for real-time operation and is capable of delivering high image quality in means of resolution and dynamic range. Various technological solutions were developed for the imaging purpose, which are introduced in detail. An example array for operation from 72 to 80 GHz is demonstrated. The imaging system hardware is introduced, along with several imaging results of humans with concealed objects.

Index Terms—Digital beamforming, microwave imaging, millimeter-wave imaging, planar arrays, sparse array.

I. INTRODUCTION

MILLIMETER-WAVE and microwave imaging systems are receiving particular interest due to their utilization in security, medical, and industrial applications. The current advances in the semiconductor technology allow for high integration densities, as well as the chance to exploit higher frequencies, i.e., millimeter-wave range and beyond. For imaging purposes, higher frequencies are demanded to achieve better lateral resolution and to provide large bandwidths necessary for better range resolution [1]. For many applications, active imaging is a necessity to achieve images with high dynamic range, and real-time operation is an ultimate goal that is usually unreachable with mechanical scanning methods [2], [3].

The state-of-the-art imaging systems capable of active real-time operation rely either on focal plane arrays [4] or reflect array technologies [5]. Focal plane arrays combined with a focusing lens or lens system suffer from low lateral resolutions and have fixed focal distances. The reflect arrays have limited bandwidths leading to poor range resolutions, and due to the dense

array design, the integration complexity becomes very high and often impractical for millimeter waves.

In this paper, a novel imaging system architecture is presented based on a planar multistatic sparse array design utilizing digital-beamforming (DBF) technique [6]. The sparse array allows for an exceptional reduction in the number of RF modules, while yet delivering high image quality. The system was designed and verified from 72 to 80 GHz and demonstrated a lateral resolution of 2 mm. The sparse array design along with simulation results is addressed in Section II. The hardware architecture and the associated calibration method are presented in Sections III and IV. The signal-processing steps involved in the image reconstruction are summarized in Section V. Measurement results and evaluations are reported in Section VI, followed by a conclusion in Section VII.

II. ARRAY DESIGN

In multistatic 2-D arrays, the antenna distributions within the transmitter aperture and the receiver aperture can be chosen separately, and are hence, designed to complement each other. The antenna distributions are preferably chosen sparse in order to reduce the system cost, measurement time, collected data volume, and power losses. The sparseness of the aperture geometry often degrades the array efficiency [7] and causes unwanted artifacts in the reconstructed images.

For a multistatic array with a transmitter aperture a_t and receiver aperture a_r, its far-field performance is given by the double convolution $a_t ** a_r$, namely, the array effective aperture [8]. In the near-field operation, however, the array performance deviates strongly and can be considerably enhanced by increasing the redundancy in its effective aperture [9]. This leads to a tradeoff between the array performance and the number of antennas, and hence, the system complexity. Besides that, careful selection of the array geometry is required in order to keep good illumination quality of the imaged object [10] and to ease its hardware realization as well.

In this study, a new array geometry is introduced, where the antennas are grouped in clusters and placed such that a 2-D dense equispaced effective aperture is achieved. Each cluster is quadratic with the antennas placed on the perimeter. This array geometry results in an effective aperture with a stepped pyramid shape, which delivers the redundancy necessary for the enhancement of the near-field operation. In this particular realization, the transmitter antenna lines are placed horizontally and the receiver antenna lines vertically. In Fig. 1, an overview of the array geometry is shown. In the array geometry, the following three different spacings are used.
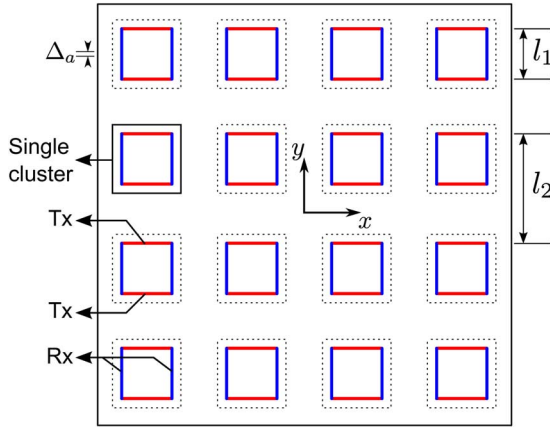
Fig. 1. Multistatic sparse array geometry with 4 × 4 clusters. Horizontal lines represent Tx positions, and vertical lines represent Rx positions.

1) The base spacing Δ_a between the antennas, which corresponds to the spacing in the effective aperture domain and is responsible for alias-free imaging. For multistatic arrays of ideal isotropic antennas, alias-free imaging is achieved with $\lambda/2$ spacing [11]. Here, Δ_a is equal to 0.75λ at 75 GHz, i.e., 3 mm, due to the limited opening angle of the used antennas, i.e., 80° half-power beamwidth (HPBW).
2) The spacing l_1 between two antenna lines within a cluster, which introduces the first sparseness in the array geometry. For n antennas per single line of a cluster, l_1 is optimally equal to $n \cdot \Delta_a$. For the proposed array, n is chosen to be equal 23 and accordingly l_1 is 69 mm.
3) The spacing l_2 of the clusters, which introduces the second sparseness in the array geometry. l_2 is optimally equal to $2n \cdot \Delta_a$, and therefore is equal to 138 mm in the proposed array.

The geometry is fully configurable depending on the selection of the cluster size and count. The cluster can be in general nonquadratic, leading to an unequal performance in x- and y-directions, which could be preferable in some applications.

In order to achieve an array aperture of around 50 cm × 50 cm, 4 × 4 clusters are used accordingly. This results in a total of 736 Tx antennas and 736 Rx antennas. Its counterpart design using a dense array, at the same base antenna spacing and array aperture size, results in 25 600 antennas. Therefore, the sparse array contains only 5.75% of that number of antennas.

The performance of the focusing quality of the array is well described by its point spread function (PSF). The PSF is simulated for a point target, followed by a backpropagation reconstruction. The PSF of the Tx array operating from 72 to 80 GHz and focusing centrally at 50-cm distance is shown in Fig. 2(a). Similarly, the PSF of the Rx array is shown in Fig. 2(b). Due to the equal aperture sizes of both arrays, the resultant lateral resolution is also equal. The target point is, however, surrounded with strong artifacts due to the introduced sparseness. As the Tx and Rx apertures are chosen to complement each other in the array effective aperture domain, the locus of the artifacts in the Tx PSF corresponds to nulls, or close to nulls, in the Rx PSF, and vice versa. The two-way PSF is given by the multiplication of the Tx PSF and the Rx PSF in space, which is shown in Fig. 3
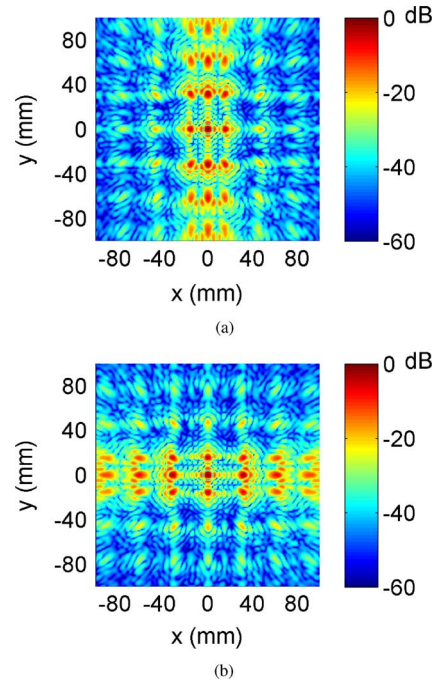

Fig. 2. PSFs for a central target 50 cm apart. (a) Tx array PSF. (b) Rx array PSF.
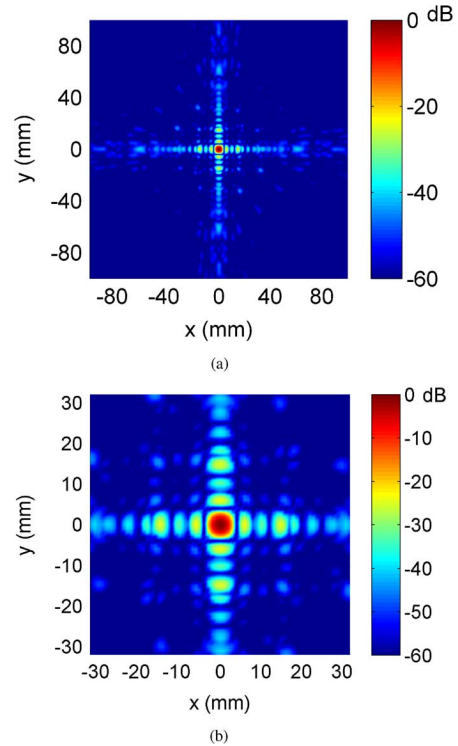

Fig. 3. Lateral two-way PSF for a central target 50 cm apart. (a) Overview. (b) Detailed view.

for the lateral plane. Fig. 4 shows the PSF along the range direction. The strong artifacts are hence suppressed, resulting in the relevant PSF for the imaging process. The two-way PSF delivers more than 60-dB suppression of the background, which is necessary for generating images with a high dynamic range.
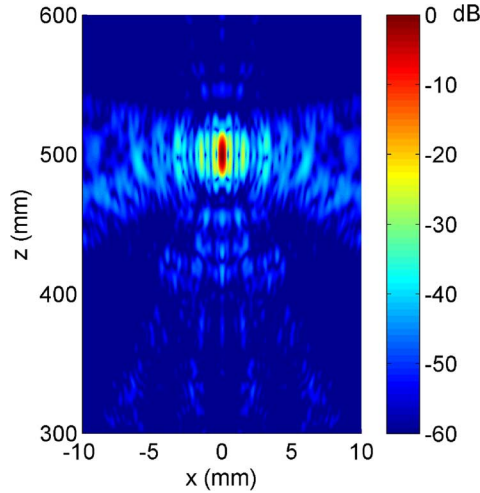
Fig. 4. Two-way PSF along range direction.

The lateral resolutions δ_x and δ_y for planar multistatic arrays are given approximately by

$$\delta_x = \frac{\lambda D}{L_x^t + L_x^r} \text{ and } \delta_y = \frac{\lambda D}{L_y^t + L_y^r} \qquad (1)$$

where D is the distance to the target measured from the plane of the phase centers of the Tx and Rx antennas, L_x^t and L_y^t are the aperture widths of the Tx array along x- and y-directions, respectively, similarly L_x^r and L_y^r are the aperture widths of the Rx array, and λ is the wavelength of the center frequency. For multistatic arrays operating with large bandwidths, the range resolution δ_z is given approximately by

$$\delta_z = \frac{c}{2\Delta F} \qquad (2)$$

where c is the speed of light, ΔF is the signal bandwidth used, and the factor 2 is due to the reflection mode. For the proposed array, operating with 8-GHz bandwidth and imaging at 50-cm distance, the lateral resolutions in x- and y-directions are 2 mm and the range resolution is 20 mm.

III. HARDWARE ARCHITECTURE

A. System Overview

The imaging system collects the reflection data coherently using stepped-frequency mode. It comprises a total number of 768 Tx channels and 768 Rx channels, whereas each of the 768 channels include 736 antennas and 32 reference channels, i.e., two reference channels per cluster. Following the DBF technique, only a single transmitter illuminates the imaged object at any time instance, and the reflected wavefront is then sampled by the receivers. The transmitters must be switched sequentially for the data collection; however, the receivers can operate in parallel. The reflection data are collected for each Tx–Rx pair and for each selected frequency, forming a 3-D data volume of $N_{\text{Tx}} \cdot N_{\text{Rx}} \cdot N_F$ complex values, where N_{Tx}, N_{Rx}, and N_F are the total number of transmitters, receivers, and stepped frequencies, respectively. Heterodyne receivers are used to allow for a high dynamic range. In this realization, 48 receiver channels can

be sampled in parallel, and hence, the receivers are multiplexed 16 times in order to collect the whole data volume. A more detailed description of the measurement system can also be found in [12].

Fig. 5(a) shows the block diagram of the imaging system. The local oscillator (LO) and RF signals are both generated from a single stable source at one-fourth of the intended frequency. These signals are distributed and quadrupled inside each cluster. The RF signal is distributed to the Tx channels, and the LO signal to the Rx channels. The mixing products in IF, i.e., 15 MHz, are digitized and processed for magnitude and phase information. IF signal digitization, signal processing, and control of the clusters with the signal source are done by the integrated signal-processing unit. This unit is customized based on a commercial PXI Express (PXIe) system, which includes PXIe controller, six eight-channel ADC units, and a field-programmable gate-array (FPGA) card, which contains the real-time capable parts of the control state machine. The proposed array of 4×4 clusters is assembled as shown in Fig. 6(a), where the front side of the clusters and the associated cooling parts are shown. Fig. 6(b) illustrates the backside of the system with its main units: signal source ①, IF switching matrices ②, signal-processing unit ③, power supply ④, and an interconnect board ⑤. The achieved measurement time for a scan with 32 frequency steps from 72 to 80 GHz is 157 ms, making it a real-time capable system for imaging humans.

B. Cluster

Each cluster contains 46 Tx antennas and 46 Rx antennas, as illustrated by the block diagram in Fig. 5(b). The hardware realization of a single cluster is shown in Fig. 7(a). The blue arrows (in online version) indicate the LO signals, and the red arrows (in online version) indicate the RF signals. The IF signals are routed through the backside of the clusters. The antennas are slightly displaced to a zigzag shape in order to ease the integration. The control of the cluster, as well as the multiplexing of the 48 IF channels to 3 IF outputs, is made by a dedicated IF switching matrix. The matrix also provides a control interface to the FPGA card of the signal-processing unit for real-time control of the antennas and the multiplexers.

Fig. 7(b) shows a disassembled cluster, which consists of an eight-layer RF printed circuit board (PCB), called an RF board, a metallic cover, and a back plate. Fig. 7(c) and (d) shows the details of the RF board. It carries distribution networks for the LO and RF signals inside the cluster, the analog front-end chips, attenuator pads for the two reference channels, and the four-layer PCB integrated part of the antenna. The analog front-end chips are mounted and wire bonded in multilevel cavities. This is preferred because the antenna feed lines, which are located on an inner layer of the PCB, should have possibly short bondwire connections in order to ensure good matching over the frequency band of operation. As the attenuation of the antenna feed lines on the PCB is considerably high, the front-end chips are placed as near as possible to the antennas. The antenna feed line length is therefore kept well below 20 mm. Manufacturing of the RF board was made possible due to current advances in the PCB manufacturing and assembly technologies, which enable routing multilevel cavities in PCBs and allow the integration of
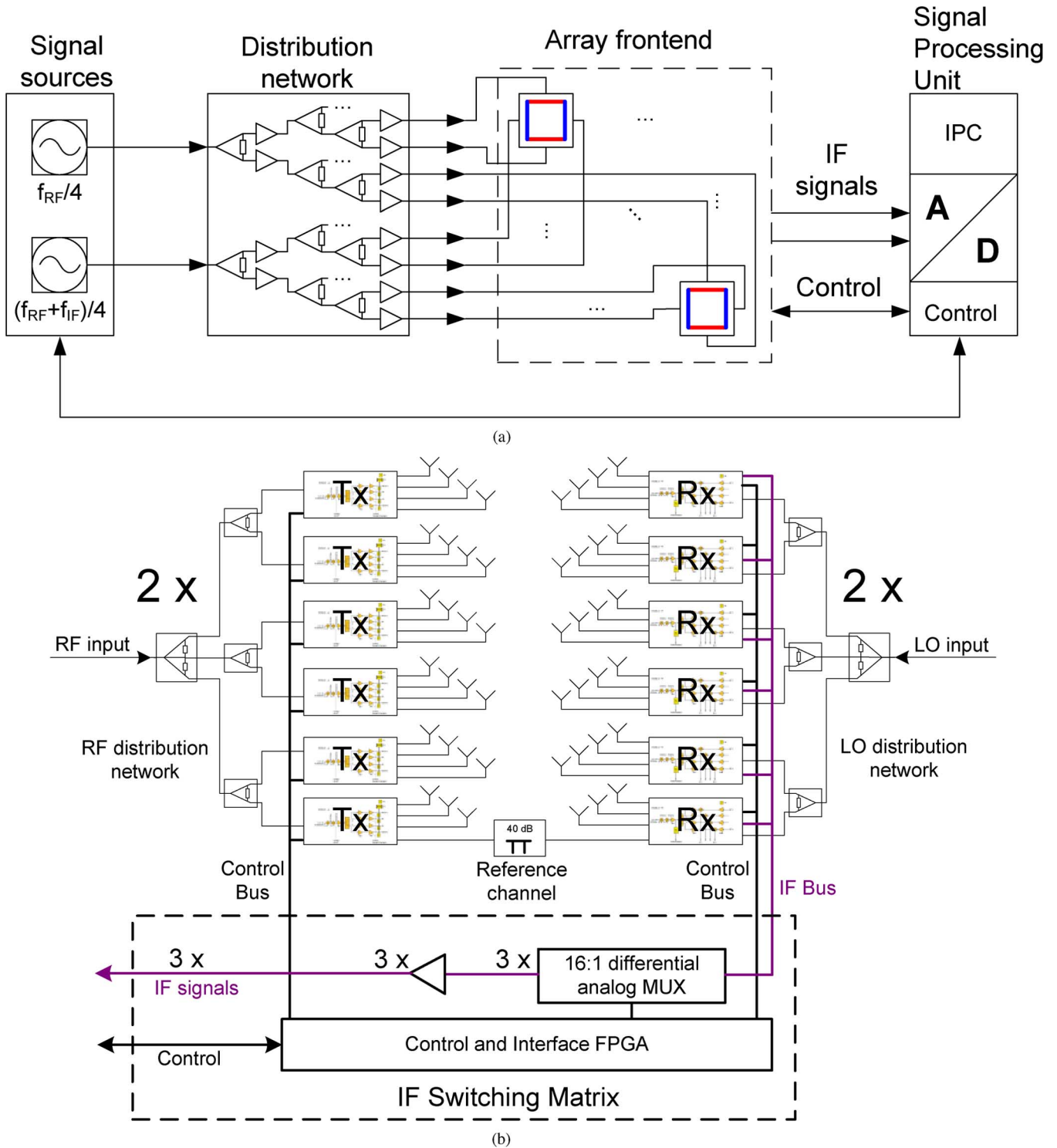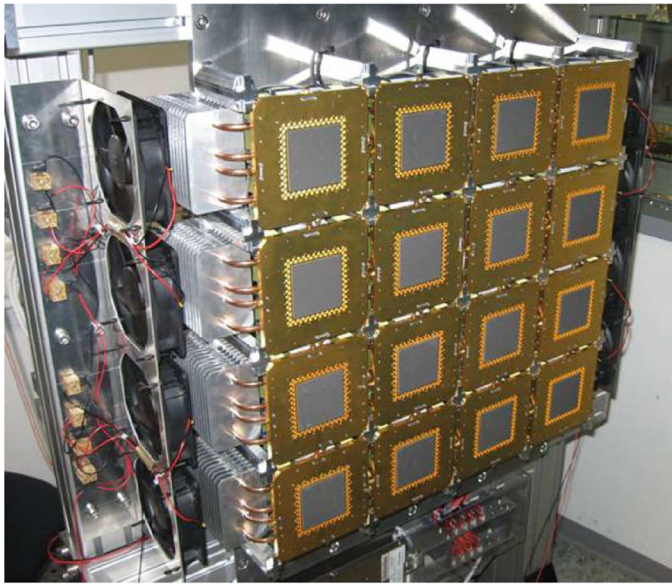
Fig. 5. Hardware block diagrams of the fully electronic imaging system. (a) System block diagram. (b) Cluster block diagram.

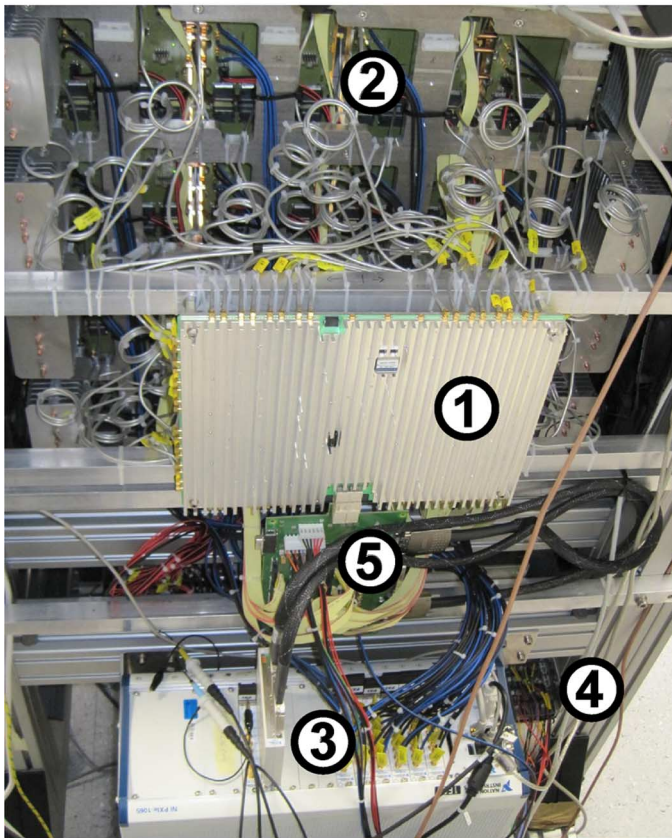surface mount devices (SMDs) along with the assembly of RF chip-on-board, all on the same PCB.

The cluster surface is formed by a gold-plated aluminum cover, for both the front and back sides, which integrates the horn part of the antenna, the connections for the LO and RF signals, and serves for electromagnetic shielding, as well as for heat transfer. The inner part of the outer surface of the cluster is prepared with an absorber sheet in order to reduce the cross-coupling between antennas and the standing waves between the imaged object and the array surface. The technical details of the chip set and antennas are detailed below.

1) Analog Front-End Chip Set: The RF front-ends are realized as custom-made monolithic microwave integrated circuits (MMICs) [13] in an industrial automotive SiGe process [14]. Fig. 8(a) and (c) shows the block diagram and a photograph of the four-channel Tx chip, respectively. The Tx chip fea-

(a)

(b)

(c)

(d)

Fig. 7. Photographs of a cluster. (a) Cluster. (b) Disassembled cluster. (c) RF board. (d) RF board detail.

(a)

(b)

Fig. 6. Fully electronic imaging system with 736 Tx and 736 Rx antennas operating from 72 to 80 GHz, showing the front and backsides of the imager. (a) Array of 16 clusters. (b) Signal generation and processing hardware.

tures an input transformer ①, an RF quadrupler, a distribution unit ②, four 80-GHz amplifier chains with matching networks and power sensors ③a–③d, and a temperature sensor ④. The quadrupler, as well as each of the amplifier chains, are controlled separately by the corresponding control signals to allow fast response times. The design of the RF matching network takes into
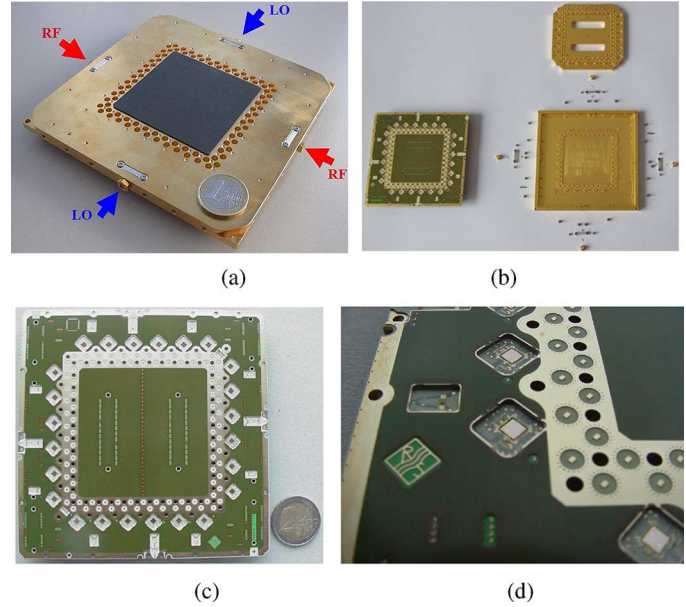
account the bond interface on the RF board. Key features of the Tx chip are as follows:

- 3-dB-bandwidth >10 GHz (76–89 GHz);
- output power >0 dBm over the frequency band;
- power consumption <600 mW at $V_{cc} = 3.3$ V;
- a die area of 4 mm^2.

Similarly, Fig. 8(b) and (d) shows the block diagram and a photograph of the four-channel Rx chip, respectively. The Rx chip features an input transformer ①, an LO quadrupler, a distribution unit with a power sensor ②, four 80-GHz LNA/mixer blocks including matching networks ③a–③d, and a temperature sensor ④. The design of the LO matching network takes into account the bond interface on the RF board as well. Key features of the Rx chip are as follows:

- 3-dB-bandwidth >10 GHz (70–82 GHz);
- conversion gain >23 dB at a single-sideband (SSB) noise figure of 9.5 dB over the frequency band;
- input 1-dB-compression point of −30 dBm;
- power consumption <650 mW at $V_{cc} = 3.3$ V;
- a die area of 4 mm^2.

2) Antenna: The presented imaging system employs linearly polarized balanced-fed patch-excited horn antennas [15]. The antenna structure uses a four-layer setup. The antenna is placed in a cavity, formed by the ground layer and a ring of via-holes. Feeding dipole and feed lines are one layer above ground. The feed lines connect the chip to the antenna without the need for vias, as the chip is mounted in a cavity, and the connection to the feed lines is done on the same PCB layer. Above the feeding dipole, two slots couple the energy to a rectangular patch, which is located at the top layer of the PCB. The horn parts of the 92 antennas, i.e., 46 Tx and 46 Rx ones, are integrated in the cover of the cluster. Reliable contact of horn and PCB part is ensured by screwing a fitting back plate against the cover. The co- and cross-polarized antenna radiation patterns are shown in Fig. 9. The plane of polarization is rotated by 45° so that polarization
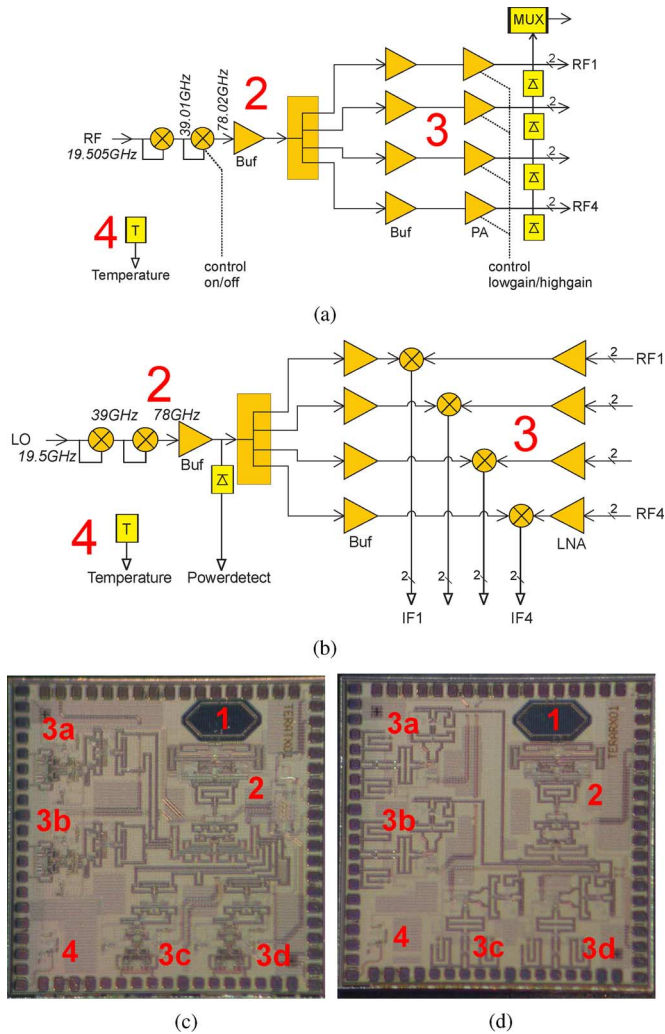
Fig. 8. Dedicated four channel analog front end chip set. (a) Tx block diagram. (b) Rx block diagram. (c) Tx chip photograph. (d) Rx chip photograph.
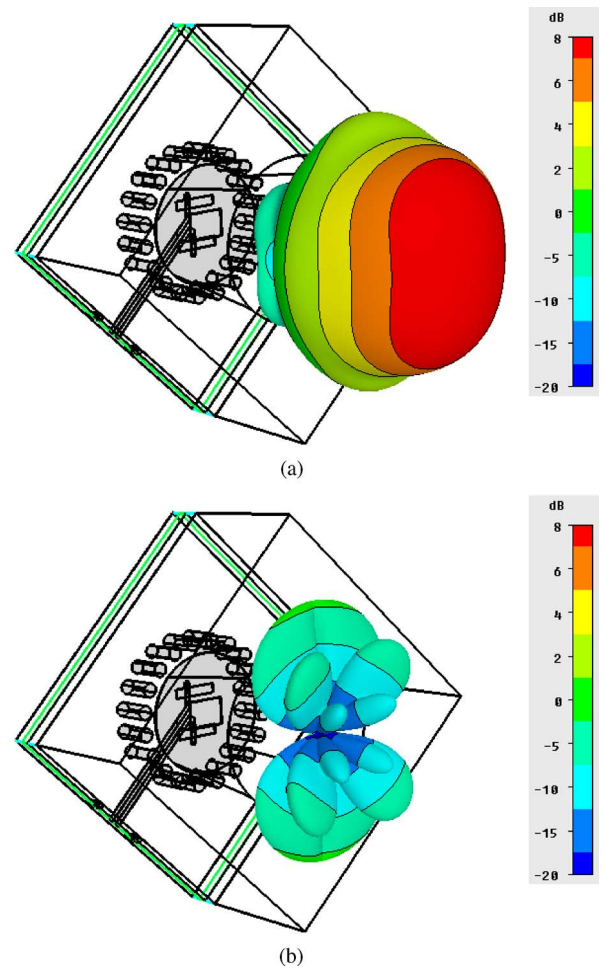

Fig. 9. Antenna radiation pattern at 75 GHz showing the radiation quality for the co-polarized component and the good suppression of the cross-polarized one. (a) Co-polarized component. (b) Cross-polarized component.

matching of Rx and Tx antennas is ensured, as well as a convenient routing of the feed lines to the chips. Key features of the antenna are as follows:

- bandwidth >10 GHz centered at 79 GHz;
- 8-dBi gain and efficiency better that −1 dB;
- return loss better than 10 dB.

C. Synthesizer

The LO and RF signals are generated using two direct digital synthesizers (DDSs) that operate from 130 to 170 MHz followed by seven multiplier/filter stages. The total multiplication factor on the synthesizer unit is 128, leading to signal range around 20 GHz. This is a compromise for the signal distribution, which is thus followed by the quadrupling to the 80-GHz range on chip. Taking this into account, the total multiplication factor to the target frequency is 512. This high multiplication factor leads to strict requirements for the frequency reference source in order to keep sufficient signal quality in terms of phase noise and spurious levels. Therefore, the clock of the two DDSs is derived from a highly stable oven-controlled crystal oscillator (OCXO). The synthesizer unit is designed for a sweep range from 17 to

21.5 GHz, i.e., leading to target frequency of 68–86 GHz covering the frequency band of interest and beyond. After the multiplier chain, the signals are distributed using Wilkinson dividers and amplified to 32 output ports for both LO and RF networks. Key specifications of the synthesizer are as follows:

- output power of 20 dBm ±3 dB for each connection;
- frequency error <200 kHz;
- statistical phase error <20° in a 20-MHz bandwidth;
- phase-noise floor <−80 dBc/Hz from 10 kHz to 20 MHz.

D. Measurement Acquisition

To record the data for image generation, one Tx illuminates the scenario after another at each frequency. The IF signal is continuously digitized and stored in the memory of the ADC unit during the complete measurement, even during switching processes when the IF signal is invalid. After the measurement is finished, the stored IF samples are processed as follows: the valid samples are selected from the memory, then digitally downconverted to baseband, and afterwards filtered by a 16-tap low-pass filter with a power bandwidth of 1.875 MHz. In order to get a phase stable signal, reference channels are used around the system. In each cluster, one selected Tx-Rx path, connected via a 40-dB attenuator pad, is used as a reference signal for all

transmitters within the same cluster. As the reference channel is treated similarly as an antenna, it is not measured continuously, but there is a time delay Δt between the measurement of the reflected wave and the reference signal. From the measured reflected waves $\underline{b}$ and the reference signals $\underline{a}$, the S-parameters are calculated using the formula [12]

$$\underline{S} = \frac{\underline{b}(t_m)}{\underline{a}(t_m + \Delta t)} \tag{3}$$

where $\underline{b}$ is the reflected wave from the scenario measured at the time t_m, and $\underline{a}$ is the reference signal from the corresponding reference channel measured at the time $t_m + \Delta t$. Due to the time delay between the measurements of the reflected waves and the reference signals, the ADC clock and synthesizer reference clock have to be synchronized and aligned carefully.

IV. System Calibration

The collected reflection data must be corrected in order to set the phase reference of the imaging system directly on the plane of the phase centers of the Tx and Rx antennas. The reflection measurements are performed on a bistatic basis, and hence, a characterization of the matching at the Tx and Rx ports is not required. Furthermore, the multiple reflections between the measured object and the array can be highly reduced by careful design of the array surface, i.e., making use of the high sparseness it includes. Therefore, the array can be calibrated by using two standards, which are chosen to be match and offset short ones. The match measurement M_m is easily realized using absorbers in front of the array aperture. The offset short measurement M_s is realized using a metal plate at a known distance. The match measurement helps to correct for the cross-coupling between the Tx and Rx antennas, whereas the offset short is used to adjust the phases of the RF channels and to equalize the magnitude of the signals over the frequency band of operation. With the known array geometry and the position of the metal plate, the reference reflections from the metal plate are simulated as Γ_s. The simulation assumes a virtual transmitter behind the metal plate according to the imaging theory [16]. For a measurement M, the object reflection Γ at the corresponding Tx–Rx pair and frequency is, hence, given by

$$\Gamma = \frac{M - M_m}{M_s - M_m} \cdot \Gamma_s. \tag{4}$$

For closely spaced Tx–Rx pairs, the cross-coupling often leads to compression in the RF receiver channel. This causes the calibration procedure to fail for this few measurements, and therefore they are masked out. Due to the selected array geometry, only less than 0.1% of the collected data volume is considered invalid. Fig. 10 illustrates an example for measured data after the system error correction of the first four clusters within the array. The reflections of the object are seen distributed over the aperture, and the high cross-coupled channels seen in the diagonal direction are masked out intentionally. The horizontal and vertical dark lines present the locations of the reference channels on each cluster, which are also masked out from the following signal-processing steps.
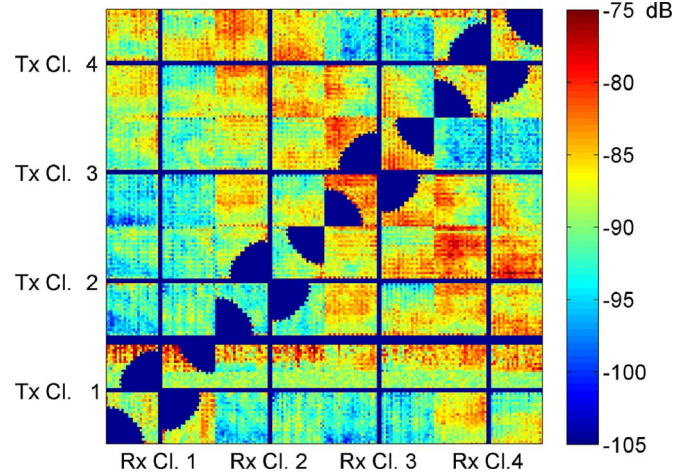

Fig. 10. Example for measured data after the system error correction, shown as the maximum value over frequency in decibel scale.

V. Signal Processing

The processing of the 3-D reflection data undergoes three main steps. First, the data are filtered using a time-gating technique in order to eliminate any residual cross-coupling within the array and to reduce the clutter signals from unwanted objects. Secondly, an illumination equalization is performed, in which the filtered data is weighted to produce a smooth effective aperture. This is necessary for the correction of the specular reflections produced on the smooth parts of the imaged object [10]. At the same step, an aperture window can be applied. Typically, a Kaiser window with low shape factor is used. In the third step, the reconstruction algorithm takes place for focusing. A numerically optimized backpropagation algorithm is used in which the signals are correlated in the space domain. Lastly, a fully focused 3-D complex image is produced.

Fig. 11 illustrates the time-domain histogram of an example measurement of a person. The histogram presents the statistical distribution of the reflected signals over the distance to the array. In this case, the main reflections exist around the 70-cm distance, and hence, the time gate was selected to include the distance from 50 to 90 cm. Some of the reflection signals are present outside this interval, which originate either from multiple reflections with the array surface itself or due to clutter of surrounding objects.

VI. Measurement Results

The imaging process is verified by screening humans. In order to avoid motion blur in the reconstructed images, the measurement must be performed fast enough. The reconstruction algorithm assumes a static scenario during the data collection, and any movement in a close order of magnitude to the used wavelengths, e.g., breathing, is sufficient to produce a blurry image. For humans standing or sitting still, measurement time of a few hundred milliseconds is sufficiently fast, which is reachable with the proposed system. The human skin is smooth relative to the millimeter waves and includes high water content, leading to strong specular reflections. This causes the illumination in the
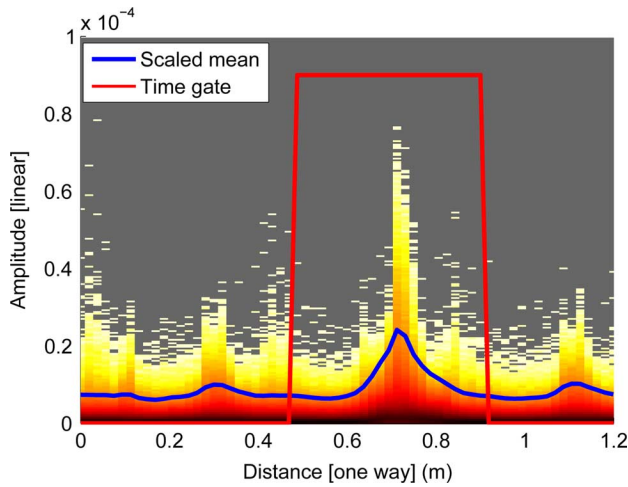
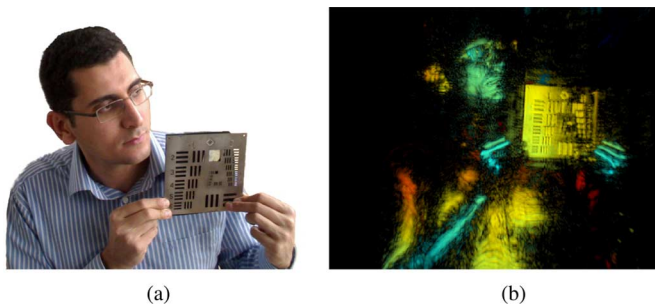Fig. 11. Time-domain histogram of an example measurement.

Fig. 12. Measurement of a person carrying USAF resolution test chart made of a metal sheet. Stepped frequencies from 72 to 80 GHz were used. The color codes the depth information. (a) Photograph (slant view). (b) Reconstructed image.

resultant image to be restricted to the skin surfaces facing the array [10], and the rest looks dark.

Fig. 12 shows the imaging result of a person carrying a U.S. Air Force (USAF) resolution test chart made of a metal sheet. The person sat approximately 50 cm from the array aperture. The associated time-domain histogram of this measurement is shown in Fig. 11. The magnitude of the 3-D image data is projected on 2-D using the maximum value along the range direction. The image is logarithmic (in decibel scale) and displaying 30-dB dynamic range. Logarithmic scale is preferable in order to emphasize the weak reflections, as well as the strong ones. The image is then colored according to the depth information. Depth is calculated as the range position where the maximum reflectivity takes place. The produced colored 2-D image assembles the 3-D information of the object, where the intensity represents the magnitude of the maximum reflectivity and the color represents the depth information with blue (in online version) for close and red (in online version) for far positions relative to the imaging system. The test chart was not facing the array completely, which helps to identify the effect of the specular reflections. As the right half was not facing the imaging array, it looks dark at its flat surface. In spite of this, the edges are well visible due to the strong diffuse reflections they produce. Another imaging result of the USAF resolution test chart is in Fig. 13, where the chart was facing the array completely and is therefore
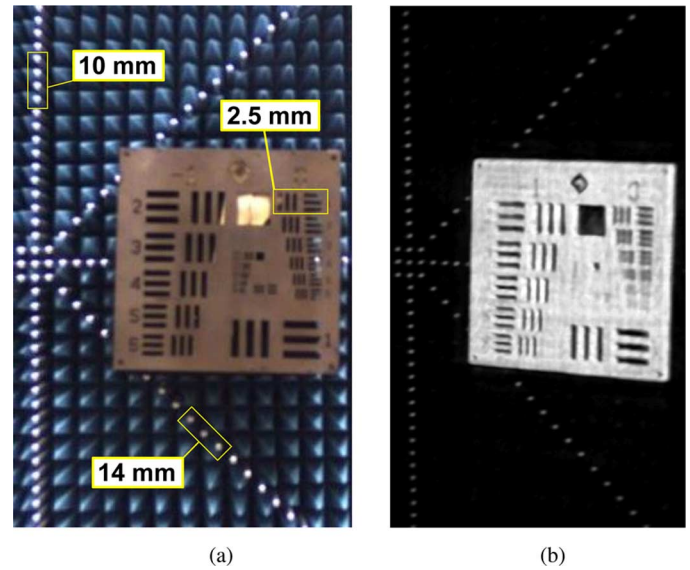

Fig. 13. Measurement of the USAF resolution test chart placed in front of a bed of nails test object prepared with pyramidal absorbers. (a) Photograph. (b) Reconstructed image.
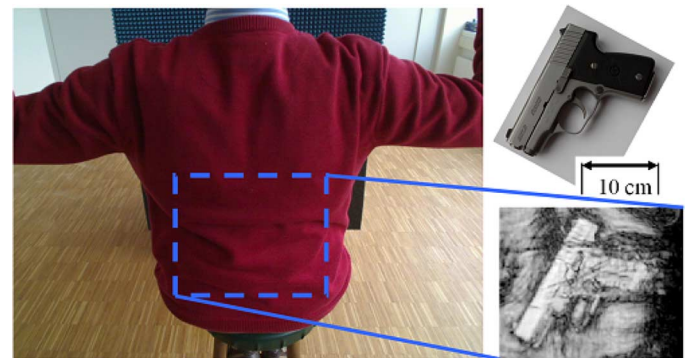

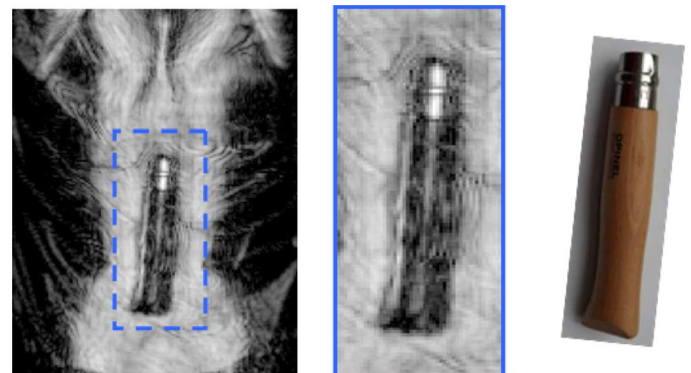Fig. 14. Measurement of a person concealing a small pistol.

Fig. 15. Measurement of a person concealing a clasp knife.

fully visible in the reconstructed image. In its background, a bed of nails was placed as a test object. It had a spacing of 10 mm in the horizontal and vertical directions, and 14 mm in the diagonal ones. All nails within the imaged volume were imaged successfully without artifacts. A 3-D rendering of the magnitude of the resultant image is shown in Fig. 13(b), prepared for a slanted

view in the horizontal plane. Lateral resolution of 2 mm is verified as well as a 30-dB alias-free image dynamic range, which meets the theoretical design of the system.

Fig. 14 shows another image result of a person while concealing a small pistol. The pistol was hidden behind a thick pullover, however it is quite visible with millimeter waves. The details of the pistol are well recognized and are present as 3-D information. Again, the logarithmic magnitude information of the projected maximum reflectivity is shown. Similarly, Fig. 15 shows an image of a concealed clasp knife on the back of a person and behind his clothing. The wooden part, as well as the metallic ones of the knife, are clearly visible.

VII. CONCLUSION

A novel imaging system architecture operating in millimeter-wave range has been introduced. The imaging system has been developed based on an optimized multistatic sparse array architecture utilizing the DBF technique. The system performance for close-range imaging has been analyzed based on electromagnetic field simulations and characterized by the evaluation of the PSF of the focused signals. The architecture of the imaging system is fully configurable to any array size. Targeting a 50 cm × 50 cm array, 16 clusters have been assembled for testing the system performance experimentally. The technological solutions used in the manufacturing of the imaging system have been described. The calibration method involved, as well as the signal processing necessary for the image preparation, have been discussed. The imaging system has been realized to operate fully electronic and to measure in real time. Verifications of the system performance have been demonstrated on humans, showing a complete agreement with the simulation results. The system demonstrates images with lateral resolution of 2 mm and 30-dB dynamic range.

REFERENCES

[1] S. S. Ahmed, A. Schiessl, and L.-P. Schmidt, "Novel fully electronic active real-time millimeter-wave imaging system based on a planar multistatic sparse array," in *IEEE MTT-S Int. Microw. Symp. Dig.*, 2011.

[2] D. M. Sheen, D. L. McMakin, and T. E. Hall, "Three-dimensional millimeter-wave imaging for concealed weapon detection," *IEEE Trans. Microw. Theory Tech.*, vol. 49, no. 9, pp. 1581–1592, Sep. 2001.

[3] K. B. Cooper, R. J. Dengler, N. Llombart, T. Bryllert, G. Chattopadhyay, E. Schlecht, J. Gill, C. Lee, A. Skalare, I. Mehdi, and P. H. Siegel, "Penetrating 3-D imaging at 4- and 25-m range using a submillimeter-wave radar," *IEEE Trans. Microw. Theory Tech.*, vol. 56, no. 12, pp. 2771–2778, Dec. 2008.

[4] A. Luukanen, A. J. Miller, and E. N. Grossman, "Active millimeter-wave video rate imaging with a staring 120-element microbolometer array," *SPIE Radar Sensor Technol. VIII and Passive Millimeter-Wave Imaging Technol. VII*, vol. 5410, pp. 195–201, 2004.

[5] P. A. Corredoura, Z. A. Baharav, B. A. Taber, and G. A. Lee, "Millimeter-wave imaging system for personnel screening: Scanning 10^7 points a second and using no moving parts," *SPIE Passive Millimeter-Wave Imaging Technol. IX*, vol. 6211, 2006, Art. ID 62110B.

[6] M. Younis, "Digital beam-forming for high resolution wide swath real and synthetic aperture radar," Ph.D. dissertation, Inst. Höchstfrequenztech. Elektron., Karlsruhe Inst. Technol., Karlsruhe, Germany, 2004.

[7] G. R. Lockwood and S. F. Foster, "Optimizing the radiation pattern of sparse periodic two-dimensional arrays," *IEEE Trans. Ultrason., Ferroelect., Freq. Control*, vol. 43, no. 1, pp. 15–19, Jan. 1996.

[8] G. R. Lockwood and S. F. Foster, "Optimizing sparse two-dimensional transducer arrays using an effective aperture approach," in *Ultrason. Symp.*, 1994, pp. 1497–1502.

[9] S. S. Ahmed, A. Schiessl, and L.-P. Schmidt, "Near field mm-wave imaging with multistatic sparse 2D-arrays," in *Eur. Radar Conf.*, Rome, Italy, 2009, pp. 180–183.

[10] S. S. Ahmed, A. Schiessl, and L.-P. Schmidt, "Illumination properties of multistatic planar arrays in near-field imaging applications," in *Eur. Radar Conf.*, 2010, pp. 29–32.

[11] M. Soumekh, "Bistatic synthetic aperture radar inversion with application in dynamic object imaging," *IEEE Trans. Signal Process.*, vol. 39, no. 9, pp. 2044–2055, Sep. 1991.

[12] A. Schiessl, S. S. Ahmed, A. Genghammer, and L.-P. Schmidt, "A technology demonstrator for a 0.5 m × 0.5 m fully electronic digital beamforming mm-wave imaging system," in *EuCAP*, 2011, pp. 2606–2609.

[13] M. Tiebout, H. Wohlmuth, H. Knapp, R. Salerno, M. Druml, J. Kaeferboeck, M. Rest, J. Wuertele, S. S. Ahmed, A. Schiessl, and R. Juenemann, "Low power wideband receiver and transmitter chipset for mm-wave imaging in SiGe bipolar technology," in *RFIC Symp.*, 2011, pp. 1–4.

[14] J. Bock, H. Schiffer, K. Aufinger, R. Stengl, S. Boguth, R. Schreiter, M. Rest, R. Knapp, M. Wurzer, W. Pemdl, T. Bottner, and T. Meister, "SiGe bipolar technology for automotive radar applications," in *Proc. IEEE Bipolar/BiCMOS Circuits Technol. Meeting*, 2004, pp. 84–87.

[15] S. Methfessel and L.-P. Schmidt, "Design of a balanced-fed patch-excited horn antenna at millimeter-wave frequencies," in *IEEE EuCAP*, 2010, pp. 1–4.

[16] C. A. Balanis, *Antenna Theory*, 3rd ed. New York: Wiley, 2005.

Sherif Sayed Ahmed (M'09) received the B.Sc. degree (with honors) in electronics and communication engineering from Cairo University, Cairo, Egypt, in 2004, and the M.Sc. degree in microwave engineering from the Technische Universität München, Munich, Germany, in 2007.

From 2007 to 2010, he was a Researcher with the Chair for Microwave Engineering and High-Frequency Technology, University of Erlangen–Nuremberg, Erlangen, Germany, where he conducted his doctoral study in the field of microwave and millimeter-wave imaging technologies in a close collaboration with Rohde & Schwarz GmbH & Co. KG, Munich, Germany. He is currently with Rohde & Schwarz GmbH & Co. KG, where he is involved with the research and development in the fields related to near-field imaging systems, standoff imaging systems, multistatic radar, advanced signal-processing techniques, terahertz technology, low phase-noise oscillators, and numerical electromagnetics. He has coauthored several conference and journal papers in the topic of microwave imaging systems.

Mr. Ahmed was the recipient of the 2007 University Academic Award of the Technische Universität München and the 2009 Innovation Award of Rohde & Schwarz GmbH & Co, KG.

Andreas Schiessl received the Dipl.-Ing. (M.Sc.) degree (with honors) in electrical engineering from the Dresden University of Technology (TUD), Dresden, Germany, in 2008, and is currently working toward the Dr.-Ing. degree in cooperation with the University of Erlangen–Nuremberg, Erlangen, Germany.

From May 2008 to May 2011, he was a Research and Development Engineer with the Network Analyzers Department, Rohde & Schwarz GmbH & Co. KG, Munich, Germany. He is currently with the newly founded Microwave Imaging Department, Rohde & Schwarz GmbH & Co. KG. He has coauthored several conference and journal papers in the topic of millimeter-wave technology. His research interest is in the area of millimeter-wave technology, focusing on millimeter-wave imaging systems, millimeter-wave measurement technology, and millimeter-wave production technology.

Mr. Schiessl was the recipient of the 2010 Rohde & Schwarz GmbH & Co. KG Innovation Award.

now CASSIDIAN), Ulm, Germany, where he later became the Head of the Corporate Advanced Microwave and Millimeter-Wave Development Department. Since 1998, he has been a Full Professor and the Head of the Chair for Microwave Engineering and High-Frequency Technology, University of Erlangen–Nuremberg, Erlangen, Germany. His research and development activities included GaAs MMIC design up to 100 GHz, millimeter-wave interconnect and packaging technologies, radar sensors, transceiver front-end technology, and antennas and in the range of 10–100 GHz. His main research interests are in the field of millimeter-wave and terahertz components and antenna technologies, as well as active and passive imaging systems, laser technology, and microwave/photonic interaction.

Dr. Schmidt is a member of VDE. He is the chairman of the German Association for Electrical Technologies (VDE)/Information Technology Society (ITG) Expert Group on Microwave Techniques. He is a member of the German IEEE Microwave Theory and Techniques (MTT)/Antennas and Propagation (AP) Chapter Commission. In 2003, he was the general chairman of European Microwave Week and the chairman of the European Microwave Conference, Munich, Germany. Until 2010, he was the German representative of the European Microwave Association (EuMA) General Assembly.

Lorenz-Peter Schmidt (M'87–SM'02) received the Diploma and Ph.D. degrees in electrical engineering from the Technical University of Aachen, Aachen, Germany, in 1974 and 1979, respectively.

From 1974 to 1979, he was with the Technical University of Aachen, as a Research Assistant, where he was concerned with the analysis of transverse discontinuities in microstrip lines. In 1979, he became a Post-Doctoral Research Associate with The University of Texas at Austin. From 1980 to 1998, he was with AEG-Telefunken (later DASA,